PHYSICAL REVIEW B **76**, 014119 (2007)

Application of x-ray excited optical luminescence to x-ray standing wave method and atomic resolution holography

Kouichi Hayashi,[1] Tetsutaro Hayashi,[1] Toetsu Shishido,[1] Eiichiro Matsubara,[2] Hisao Makino,[3]
Takafumi Yao,[4] and Tomohiro Matsushita[5]
[1]*Institute for Materials Research, Tohoku University, Sendai 980-8577, Japan*
[2]*Department of Materials Science, Kyoto University, Kyoto 606-8501, Japan*
[3]*Kochi University of Technology, Mika-gun, Kochi 782-8502, Japan*
[4]*Center for Interdisciplinary Research, Tohoku University, Sendai 980-8578, Japan*
[5]*Japan Synchrotron Radiation Research Institute (JASRI), SPring-8, 1-1-1 Kouto, Sayo-cho, Sayo-gun, Hyogo 679-5198, Japan*
(Received 13 September 2006; revised manuscript received 22 April 2007; published 26 July 2007)

X-ray excited optical luminescence (XEOL) was applied to the x-ray standing wave (XSW) method and atom-resolved x-ray holography (XH). We measured the incident beam angular dependence of the luminescence intensity from a ZnO-coated Al_2O_3, and found that it corresponded to the XSW/XH pattern of Al_2O_3. The present result demonstrates that hard x-ray XSW/XH studies for light elements, which have been difficult by fluorescence detection, can easily be carried out by XEOL detection.

DOI: 10.1103/PhysRevB.76.014119 PACS number(s): 42.40.−i, 68.49.Uv, 78.55.−m, 85.30.−z

I. INTRODUCTION

When x rays are irradiated on solids, scattering x rays, fluorescent x rays, photoelectrons, and Auger electrons are typically emitted. In addition, some materials emit visible infrared or ultraviolet rays; this phenomenon is called x-ray excited optical luminescence (XEOL). In the 1960s, XEOL was observed in alkali halides and oxides including dilute rare earths.[1–3] XEOL has been applied to x-ray absorption fine structure (XAFS) studies. In 1978, Bianconi *et al.* reported that the XAFS spectrum around the Ca*K* absorption edge of CaF_2 was measured by detecting its XEOL.[4] In 1993, Sham *et al.* conducted XEOL XAFS studies on porous Si and made it possible to understand the mechanism of luminescence emission.[5] In 2001, Ishii *et al.* measured the XAFS spectra of optically active Er in a Si wafer separately from those of nonactive Er.[6]

As described above, XEOL has been applied to site-selective XAFS measurements, whereas XAFS techniques using x-ray fluorescence and transmittance cannot be used for such measurements. On the other hand, the x-ray standing wave (XSW) method[7,8] and atomic-resolution x-ray holography (XH),[9] which together enable us to determine the local structure around a specified atom, normally use x-ray fluorescence from the specified atom, but there has been no report on the use of XEOL to date. By detecting x-ray fluorescence, the XSW method and internal detector XH[10] are used to measure the intensities of the electromagnetic fields of x rays at fluorescing atoms; these intensities are modulated by the interference between direct and scattered x rays. The XSW/XH pattern can be regarded as an angular anisotropy of absorption of the specific element in the sample, since the absorption is proportional to the intensity of the electromagnetic field at the atom locations. Taking this idea into account, it follows that the intensity of XEOL depends on the x-ray absorption of the sample in principle, and its angular dependence provides the XSW/XH pattern. To verify this assumption, we measured the XEOL intensity variation of a ZnO-coated sapphire single crystal with a change in the incident beam direction, and we discuss the possibility of XSW/XH measurements.

II. CONCEPT

Let us consider the principles of the XSW method and internal detector XH, using Fig. 1(a). An x ray directly hitting a target atom interferes with an x ray scattered by neighboring and/or distant atoms, and the target atom senses the electromagnetic field at its location. If the x-ray energy is higher than the x-ray absorption edge, the target atom emits x-ray fluorescence commensurate with the intensity of the electromagnetic field. XEOL experiments also involve the

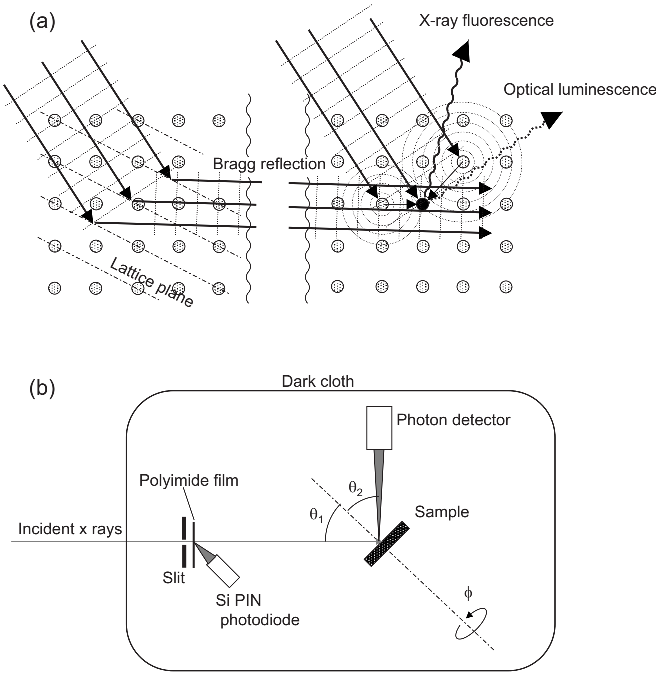

FIG. 1. (a) Principles of XSW method and XH by detection of XEOL and (b) experimental setup for XSW/XH measurement.

excitation of a core electron. The core hole then relaxes through a complex series of radiative or nonradiative processes. Luminescence may occur from higher excited states by secondary photoemission, inelastic scattering from Auger electrons or photoelectrons, and other secondary processes occurring during the relaxation of a core hole. All of these processes may contribute to the observed signal, and this is a significant difference between XEOL and x-ray fluorescence. Thus, the emission center involves an atom different from that of the x-ray absorber, in which case there is an interionic energy transfer. In the XSW/XH measurement by XEOL, all absorber atoms become targets, as shown in Fig. 1(a). However, if the sample is composed of multiple elements, the contribution of the luminescence intensity to each element depends on its content and absorption coefficient. In the case of Al_2O_3 used in the present work, the contribution of Al is 30 times larger than that of O, because the O atom has a much smaller absorption cross section. Thus, XSW/XH measurements for these samples provide the locations in the unit cells and local structures around Al atoms.

III. EXPERIMENTAL

Here, we adopted an Al_2O_3 (sapphire) single crystal coated by a ZnO epitaxial film[11] as a sample, because XEOL is known to occur for sapphire.[12] The sample size was $4 \times 4 \times 0.5$ mm^3. The XSW/XH experiment was conducted at undulator beamline BL37XU in the SPring-8 synchrotron radiation facility. Incident x rays were monochromatized using a Si 111 monochromator. Figure 1(b) shows the experimental setup used in this study. Since the intensity of luminescence selected by a grating monochromator was too weak for an XSW/XH pattern to be observed, the luminescence was detected directly using a photon counter (Hamamatsu Photonics H8259), which was set on the 2θ arm of a goniometer.[13] This counter was sensitive to photons with a wavelength of 185–680 nm. To avoid the detection of the fluorescent and scattered x rays from the sample, a 2-mm-thick quartz glass was set in front of the detector. Moreover, the photon counter was covered by a black box to avoid the detection of stray light. To monitor the incident beam intensity, scattered x rays from the polyimide film were detected using a Si PIN diode in current mode. The sample was mounted on a two-axis rotatable stage. The equipment was enclosed by a dark cloth to suppress the noise of the detector; the cloth substantially suppressed the background intensity (1000 photons/s). The incident x-ray energy was 15.0 keV. The luminescence intensities were obtained as a function of azimuthal angle ϕ and polar angle θ_1 within the ranges of $0° \leq \phi \leq 360°$ and $0° \leq \theta_1 \leq 48°$. The ϕ rotation speed was 0.3°/s, and luminescence intensity was integrated over data for a 0.1 s sampling time. θ_1 was rotated discretely in step of 1.0°. The luminescence exit angle of θ_2 was fixed at 45°. The total number of pixels was 57 600. The measurement time was about 2 h. The luminescence intensity obtained by subtracting the background from the measured intensity was about 600 000 photons at each pixel.

IV. RESULTS AND DISCUSSION

Before the XSW/XH experiment, we measured the XEOL spectra of the ZnO/Al_2O_3 sample using a grating spectrometer (JASCO CT-10S) to check the effects of the ZnO overlayer, as shown in Fig. 2. The overall shape of the XEOL spectrum is quite different from that of the photoluminescence spectrum emitted from the ZnO layer.[14] Kristianpoller *et al.* observed a broad peak at 400 nm in the photoluminescence spectra of a sapphire,[12] which is also seen in the XEOL spectrum in Fig. 2. This reveals that most of the XEOL observed here originated from the sapphire substrate. We also checked the XEOL spectrum from a pure sapphire and confirmed that it was almost the same as that from the ZnO/Al_2O_3 sample. 97% of incident x rays were calculated to pass through the ZnO layer.

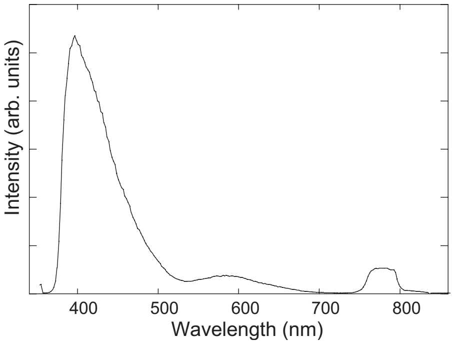

FIG. 2. XEOL spectra from ZnO/Al_2O_3.

Figure 3(a) shows angular anisotropies of the XEOL intensity. The pattern in Fig. 3(a) exhibits clear XSW lines, implying that XSW/XH data were recorded by the XEOL detection. The XSW lines in Fig. 3(a) can be assigned in accordance with our knowledge of the crystal structures of bulk Al_2O_3. We also measured a simple single crystal sapphire (Al_2O_3), which was of the same size as the ZnO/Al_2O_3 sample, by XEOL in order to examine the effect of the ZnO overlayer. Very weak XSW lines similar to those in Fig. 3(a) were observed; however, their amplitudes were more than ten times smaller than those obtained from the ZnO-coated Al_2O_3. This is attributed to the following reason. The emission band at 400 nm from the sapphire was due to the F center, which is an oxygen-ion vacancy occupied by two electrons. Thus, the intensity of this band increases with the concentration of oxygen vacancies.[12,15] Assuming that the oxygen vacancies were distributed uniformly in the sapphire, we calculated the hologram while taking into account the extinction effect.[16] In the calculated hologram, the intensities of the XSW lines were as weak as those observed from the simple single-crystal sapphire. In this case, all the x rays are absorbed by the sapphire and converted into luminescence, regardless of the incident-beam direction because of its large thickness. The only effect appears to be the angular dependence of extinction due to scattering, because some scattered x rays go outside the sample region. Since the kind of problem with sample thickness has also been seen in XEOL XAFS studies using thick samples, thin samples were prepared in those studies.[17] The appearance of the strong XSW lines in Fig. 3(a) can be understood on the basis of the assumption that the luminescence was emitted intensively from a thin region of Al_2O_3 close to the ZnO/Al_2O_3 interface, where a large number of oxygen vacancies might have formed on the sapphire surface during MBE.

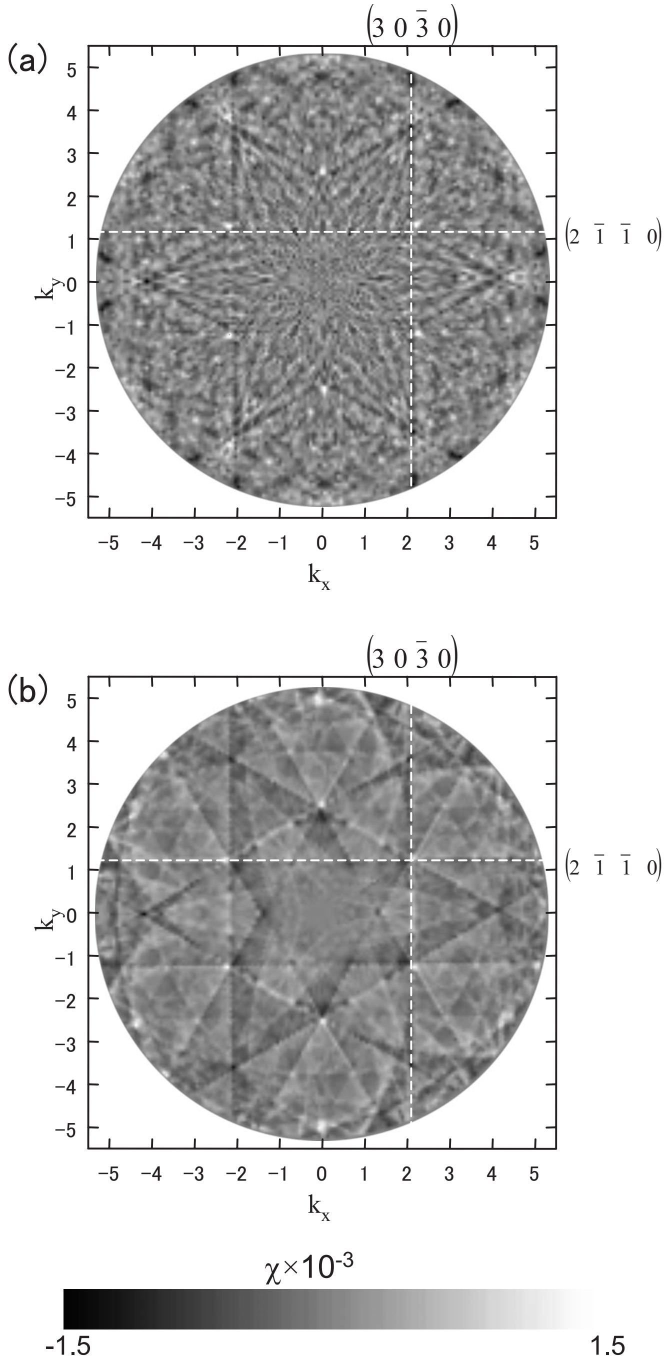

FIG. 3. (a) Experimental and (b) calculated XSW/XH patterns produced by luminescence from ZnO/Al_2O_3. The patterns are displayed in the k_x-k_y plane using the relations $k_x=|\mathbf{k}|\cos\phi\cos\theta$ and $k_y=|\mathbf{k}|\sin\phi\sin\theta$, where $\mathbf{k}$ is the wave number of the incident x rays. The luminescence intensity was normalized with respect to the incident x-ray intensity. The normalized luminescence intensity $I(\theta_1,\phi)$ was transformed into $\chi(\theta_1,\phi)$ using the equation $\chi(\theta_1,\phi)=[I(\theta_1,\phi)-I_0]/I_0$, where I_0 is the average intensity over the whole ϕ scan range.

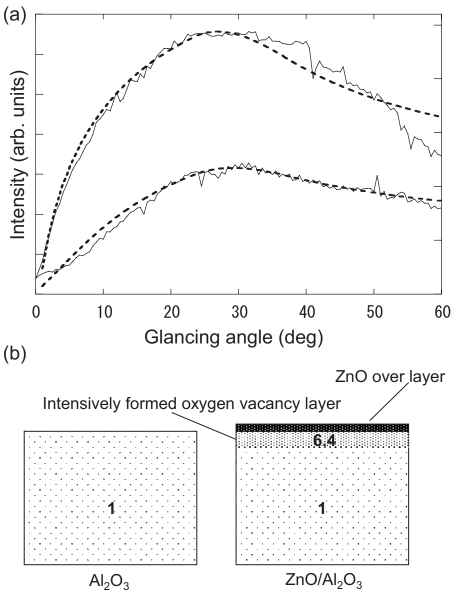

FIG. 4. (a) Incident x-ray beam angle dependence of luminescence intensities for ZnO/Al_2O_3 (upper curve) and pure Al_2O_3 (lower curve), and (b) their derived structure models. The background intensities were measured and subtracted from the measured XEOL intensities. The abscissa in (a) indicates angles between the incident x-ray beam and the sample surface. Broken lines in (a) indicate the intensity variations calculated using the model in (b). The calculations include the effects of beam size and sample surface area. The figures of 1 and 6.4 in the structure models indicate the relative concentrations of the oxygen vacancies. A rotating anode tube with a Mo target was used for the x-ray source. The Mo$K\alpha$ line was monochromatized and focused on the samples by curved graphite.[18] The sample was mounted on a rotation stage. The focal spot was 2.0 mm in diameter. The XEOL was measured by the photon counter used for the XSW/XH experiment in SPring-8.

To confirm this assumption, we measured the incident beam angle dependence of the XEOL intensity for both ZnO/Al_2O_3 and pure Al_2O_3. Figure 4(a) shows the angular dependence of the XEOL intensity. The upper and lower solid lines indicate XEOL intensities from ZnO/Al_2O_3 and pure Al_2O_3, respectively. The XEOL intensity from the ZnO/Al_2O_3 is about twice that from the pure Al_2O_3. Moreover, its increment in the lower glancing angle region was higher than that of the pure Al_2O_3, implying that the luminescence was emitted from the upper region of the Al_2O_3 substrate. Dotted lines indicate the calculated XEOL intensities. In the calculation for the pure Al_2O_3, we adopted a sample model in which the oxygen vacancies were distributed uniformly. The calculation results obtained using this model fitted the measured data well. In the calculation for the ZnO/Al_2O_3, we assumed the existence of a shallow Al_2O_3 region, in which the oxygen vacancies were intensively formed, in addition to the uniform oxygen vacancy distribution of the pure Al_2O_3 model. In the calculations, the thickness and the concentration of the oxygen vacancies relative to those of the pure Al_2O_3 model were varied for the upper layer in order to fit the calculated curve to the experimental one. The best fit depicted in Fig. 4(a) was obtained when the thickness and the concentration relative to that of the pure Al_2O_3 model were 65 μm and 6.4, respectively. The oxygen vacancy distribution model is shown in Fig. 4(b). Although this is a very simple model, it can sufficiently explain the observed XSW/XH pattern.

Using this oxygen vacancy distribution model of ZnO/Al_2O_3, the calculation of the XSW/XH pattern was carried out as shown in Fig. 3(b). Here, we adopted a calculation technique based on diffraction structure factors instead of the real space summation of point scatters, which is limited to a small cluster (−10 nm). Moreover, the calculation took into account the extinction effect based on the power transfer equation. Details of these calculation methods are described in Ref. 16. X rays absorbed by Al and O atoms were assumed to cause the luminescence emissions. However, since the absorption cross section f'' of the Al atom is about 30 times larger than that of the O atom at this x-ray energy, the contribution of Al atoms is considered to be dominant. Since the luminescence light was optically transparent to the 0.5-mm-thick sapphire, the escape depth of the luminescence was assumed to be infinite. The calculated pattern well reproduces the experimental one. From the pattern in Fig. 3(b), it is known that the strongest XSW lines were the $(30\bar{3}0)$ line or equivalent lines, and they are markedly observed in Fig. 3(a). To estimate the validity of this calculation more exactly, the $(30\bar{3}0)$ lines in Figs. 3(a) and 3(b) were averaged over the k_y direction,[19] as shown in Fig. 5(a). Both of the obtained XSW line profiles show sinusoidal signals at specific k_x=2.3 Å^{-1}, which are typically seen in XSW studies. The position and amplitude of the experimental pattern well agree with those of the calculated pattern. Since the effect of the Bragg reflections other than the $(30\bar{3}0)$ reflection still remains slightly, the theoretical XSW profile is still noisy as in the case of the experimental one. As mentioned above, the contribution of the Al atoms is dominant in the formation of the XSW profiles. Thus, the phase is interpreted as the term of the positions of Al atoms. Strictly speaking, the shape of the luminescence yield curve during the Bragg reflection should be estimated by the established XSW theory using the dynamical diffraction approximation.[7,8] However, since the present measurement was not conducted with a fine angular step ($\sim 10^{-3}$°), unlike the case with the conventional XSW measurement, this method was hardly applicable. To circumvent this problem, we adopted the kinematical XSW approximation here. Tolkiehns *et al.* reported that the XSW profile shapes of both sides of a Bragg reflection can be explained by the kinematical XSW approximation and that they are affected by the emitting atom position in the unit cell.[20] On the basis of their result, we found that the measured XSW profile surely reflected the Al position. Figure 5(b) shows a sketch of the atomic arrangement of Al on the (0001) plane. The wave field due to the XSW forms the planar interference along the direction of the reciprocal lattice space vector of $\mathbf{H}_{30\bar{3}0}$. Its period coincides with half of the Al-Al distance. From the relationship between the atomic arrangement and the wave field pattern drawn in Fig. 5(b), we can see that all Al atoms lie on the interference planes. Therefore, the phases of the wave field at all Al atom locations are equal. This provides the maximal yield variation. The present result proved that XSW measurement using the luminescence yield, as well as using fluorescence or Auger electrons, is possible.

Next, we applied the Barton algorithm[21] to the pattern in Fig. 3(a) to reconstruct the atomic images. However, this was not successful because of the single-energy hologram and limited scan range ($\theta \leqslant 48°$) during hologram measurement. Therefore, we used a scattering pattern extraction algorithm (SPEA) using the maximum-entropy method (MEM).[22] This technique is very powerful for real-space reconstruction from a single energy photoelectron hologram. The algorithm can be extended to x-ray holography by replacing the scattering pattern matrix for the electron holography with that for the x-ray holography. The hologram amplitude at the incident beam of $\mathbf{k}_i$ can be approximated as

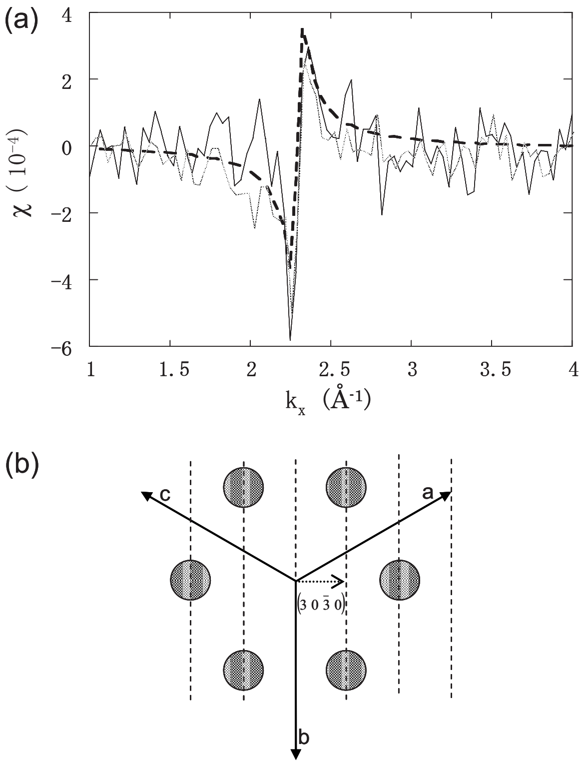

FIG. 5. (a) XSW line profile averaged over the k_y direction and (b) sketch for explaining relation ship between atomic arrangement and interference x-ray field. Solid and dotted lines in (a) indicate the profiles obtained from Figs. 3(a) and 3(b), respectively. The broken line in (a) is the XSW curve calculated including only the $(30\bar{3}0)$ reflection effect; and it serves as visual line. Circles in (b) indicate Al atoms on the (0001) plane in Al_2O_3. Dotted lines in (b) show the antinode of the XSW.

$$\chi(\mathbf{k}_i) = \sum_h [|\Psi_{\mathbf{a}_h}(\mathbf{k}_i)|^2 + \Phi_0^*(\mathbf{k}_i)\Psi_{\mathbf{a}_h}(\mathbf{k}_i) + \Phi_0(\mathbf{k}_i)\Psi^*_{\mathbf{a}_h}(\mathbf{k}_i)], \tag{1}$$

where $\Phi_0(\mathbf{k}_i)$ and $\Psi_{\mathbf{a}_h}(\mathbf{k}_i)$ are the reference wave function and the object wave function scattered by the atom located at $\mathbf{a}_h$, respectively, and h is the integer index for an atom. Then the equation is extended as

$$\chi(\mathbf{k}_i) = \sum_j t_{\mathbf{a}_j}(\mathbf{k}_i) \cdot G_j, \tag{2}$$

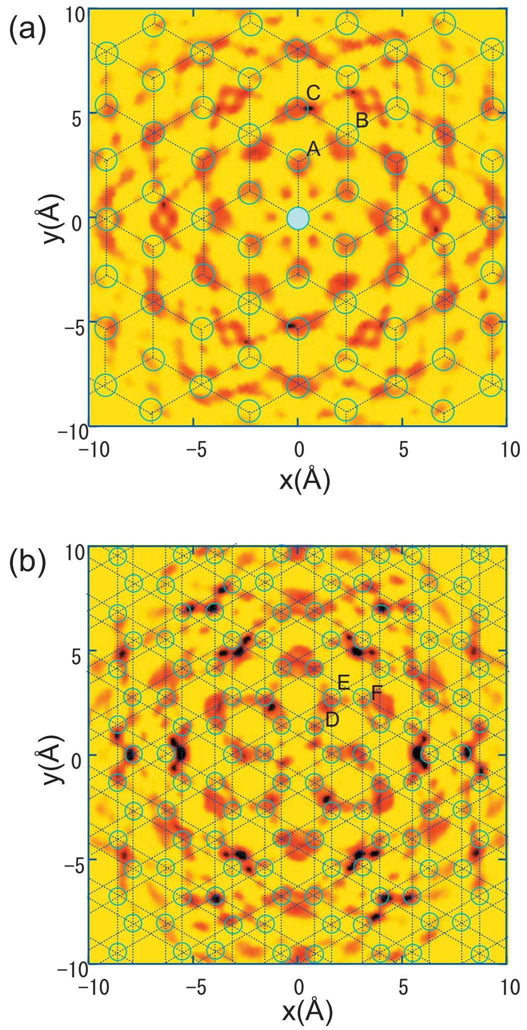

FIG. 6. (Color) Real-space images reconstructed from hologram in Fig. 3(a) by SPEA-MEM. The planes parallel to the {001} lattice plane cutting through the emitter atom, 1.1 Å above the Al atom, are displayed in (a) and (b), respectively. Circles in (a) and (b) indicate theoretical Al and O positions, respectively.

$$t_{\mathbf{a}_j}(\mathbf{k}_i) = |\mathbf{a}_j|[|\Psi_{\mathbf{a}_j}(\mathbf{k}_i)|^2 + \Phi_0^*(\mathbf{k}_i)\Psi_{\mathbf{a}_j}(\mathbf{k}_i) + \Phi_0(\mathbf{k}_i)\Psi_{\mathbf{a}_j}^*(\mathbf{k}_i)], \tag{3}$$

where $t_{\mathbf{a}_j}(\mathbf{k}_i)$ is defined as the scattering pattern function, representing the holographic pattern caused by an atom located at $\mathbf{a}_j$. Here, $M(200\times200\times200)$ mesh voxels are defined to represent a real space in the range of $20\times20\times20$ Å^3. The value for the voxel at $\mathbf{a}_j$ is expressed by G_j (with j as an integer index), and it represents the occupation of scatterer atoms. The number of $\mathbf{k}_i$ parameters N corresponds to the amount of the measured hologram pixels (57 600). Thus, the term $t_{\mathbf{a}_j}(\mathbf{k}_i)$ forms the scattering pattern matrix $\mathbf{T}$, and Eq. (2) can be regarded as a simple linear relation given by

$$\chi = \mathbf{T}\cdot\mathbf{G}, \tag{4}$$

where χ and $\mathbf{G}$ are arrays composed of $\chi(\mathbf{k}_i)$ and G_j, respectively. Since the number of known data N is much smaller than that of unknown data M, the equation is difficult to solve using conventional gradient methods. We adopt an iterative-scaling maximum-entropy method for the inverse calculation of the linear equation. The entropy utilized here is defined as

$$S = -\sum_j G_j^{(n)} \ln \frac{G_j^{(n)}}{G_j^{(n-1)}} - \lambda C, \tag{5}$$

$$C = \frac{1}{N}\sum_i \frac{\left|\chi_i - \sum_j t_{\mathbf{a}_j}(\mathbf{k}_i)G_j\right|^2}{\sigma_i^2} - 1, \tag{6}$$

where n is an index for iteration and σ_i is the standard deviation of the noise. The entropy S is maximized to obtain the real-space voxel, i.e., the three-dimensional real-space image. Before applying the SPEA-MEM to the present data, we estimated its performance using theoretical and experimental Au holograms, and confirmed that the real-space images were markedly improved in comparison with those obtained using the Barton algorithm.[23] Marchesini and Fadley also imaged the atoms from theoretical two-energy x-ray holograms by such a fitting-based reconstruction technique.[24]

Figures 6(a) and 6(b) show the obtained real space images for the (0001) plane at $z=0.0$ and 1.1 Å, in which Al and O atoms exist, respectively. Analogous to the XSW analysis described above, the central atom in Fig. 6(a) can be regarded as Al, since the contribution of the Al atoms to the XEOL intensity was much larger than that of O atoms. Circles in Figs. 6(a) and 6(b) indicate theoretical positions of Al and O atoms, respectively. Al occupies two distinct sites in the (0001) plane, and therefore, two types of environments are overlapped in Fig. 6. From the resulting atomic images, neighbor Al atoms indicated by A, B, and C are successfully reconstructed, although the image of atom B shifts toward the origin. In addition, oxygen atoms seem to be reconstructed despite the smallness of their scattering cross sections. The rings formed by the connections among the neighbor atoms indicated by D, E, F and their equivalents are certainly observed in Fig. 6(b). However, the real-space image on the O plane is generally blurrier than that on the Al plane, because of the complex atomic arrangement and small x-ray scattering cross section of the Al atom. Atomic images of regions further than 7 Å from the origin are not clearly reconstructed from the present hologram data. This will be resolved by the multiple energy holography method and a wide scan range.

V. CONCLUSION

We measured the incident beam angular anisotropy of the luminescence intensity from a ZnO-coated sapphire, and successfully obtained the XSW/XH data. The calculated pattern of Al_2O_3, which included the intensively formed oxygen vacancy layer, obtained using the extinction effect reproduced a XSW profile whose amplitude and phase fit the experimental ones well. Moreover, the Al and O atoms were reconstructed using SPEA-MEM. The XSW/XH measurement using x-ray fluorescence is generally difficult for light elements, such as Al or Si, because of their small cross sections for inner-shell ionization and the absorption of their fluorescence by air. Our results demonstrate that hard x-ray XSW/XH measurement is possible for light elements using XEOL.

ACKNOWLEDGMENTS

We thank Y. Terada for her technical help. She made the dark cloth for the XEOL XSW/XH experiment. This work was performed under the approval of the SPring-8 Program Advisory Committee (2004A0041-NXb-np-Na), and was supported by the Industrial Technology Research Grant Program in 2000 of the New Energy and Industrial Development Organization (NEDO) of Japan. Part of this work was financially supported by a Grant-in-Aid for Scientific Research (B) (Grant No. 15360329) and for young scientists (Grant No. 15686025) from the Ministry of Education, Culture, Sports, Science and Technology.

[1] R. C. Linares, J. B. Schroeder, and L. A. Hurlbut, Spectrochim. Acta **21**, 1915 (1965).
[2] A. P. D'Silva, E. L. Dekalb, and V. A. Fassel, Anal. Chem. **42**, 1847 (1970).
[3] M. N. Kabler and D. A. Patterson, Phys. Rev. Lett. **19**, 652 (1967).
[4] A. Bianconi, D. Jackson, and K. Monahan, Phys. Rev. B **17**, 2021 (1978).
[5] T. K. Sham, D. T. Jiang, I. Coulthard, J. W. Lorimer, X. H. Feng, K. H. Tan, S. P. Frigo, R. A. Rosenberg, D. C. Houghton, and B. Bryskiewicz, Nature (London) **363**, 331 (1993).
[6] M. Ishii, Y. Tanaka, T. Ishikawa, S. Komuro, T. Morikawa, and Y. Aoyagi, Appl. Phys. Lett. **78**, 183 (2001).
[7] I. A. Vartanyants and M. V. Kovalchuk, Rep. Prog. Phys. **64**, 1009 (2001).
[8] M. J. Bedzyk and G. Materlik, Phys. Rev. B **32**, 6456 (1985).
[9] P. M. Len, T. Gog, C. S. Fadley, and G. Materlik, Phys. Rev. B **55**, R3323 (1997).
[10] T. Gog, P. M. Len, G. Materlik, D. Bahr, C. S. Fadley, and C. Sanchez-Hanke, Phys. Rev. Lett. **76**, 3132 (1996).
[11] Y. Chen, H. Ko, S. Hong, and T. Yao, Appl. Phys. Lett. **76**, 559 (2000).
[12] N. Kristianpoller, A. Rehavi, A. Shmilevich, D. Weiss, and R. Chen, Nucl. Instrum. Methods Phys. Res. B **141**, 343 (1998).
[13] K. Hayashi, M. Miyake, T. Tobiaki, Y. Awakura, M. Suzuki, and S. Hayakawa, Nucl. Instrum. Methods Phys. Res. A **467/468**, 1241 (2001).
[14] K. Hayashi, T. Hayashi, T. Shishido, E. Matsubara, H. Makino, and T. Yao, Bunseki Kagaku **55**, 441 (2006).
[15] K. H. Lee and J. H. Crawford, Jr., Phys. Rev. B **15**, 4065 (1977).
[16] P. Korecki, D. V. Novikov, M. Tolkiehn, and G. Materlik, Phys. Rev. B **69**, 184103 (2004).
[17] S. Emura, T. Moriga, J. Takizawa, M. Nomura, K. R. Bauchspiess, T. Murata, K. Harada, and H. Maeda, Phys. Rev. B **47**, 6918 (1993).
[18] Y. Takahashi, K. Hayashi, K. Wakoh, N. Nishiki, and E. Matsubara, J. Mater. Res. **18**, 1471 (2003).
[19] K. Hayashi, Phys. Rev. B **71**, 224104 (2005).
[20] M. Tolkiehn, D. V. Novikov, and S. S. Fanchenko, Phys. Rev. B **71**, 165404 (2005).
[21] J. J. Barton, Phys. Rev. Lett. **61**, 1356 (1988).
[22] T. Matsushita, A. Yoshige, and A. Agui, Europhys. Lett. **71**, 597 (2005); **71**, 877 (2005).
[23] T. Matsushita and K. Hayashi (unpublished).
[24] S. Marchesini and C. S. Fadley, Phys. Rev. B **67**, 024115 (2003).